High-frequency Resonance Analysis and Impedance Reshaping Control of MMC-HVDC System Based on Frequency Coupling Impedance Model

Juanjuan Wang, Wei Chen, Yuekun Liu, Chuang Fu, Yunming Ye, and Junjie Feng

***Abstract*—In recent years, high-frequency resonance (HFR) events occurred in several modular multilevel converter based high-voltage direct current (MMC-HVDC) projects. The time delay of an MMC-HVDC system is the critical factor that induces HFR. The frequency coupling affects the impedance characteristics of an MMC and further deteriorates system stability. Therefore, in this paper, a multi-input multi-output admittance model of an MMC-HVDC system is developed to analyze its frequency characteristics. The effects of current loop, power loop, phase-locked loop, and operating point on the MMC frequency coupling degree are analyzed in detail. Meanwhile, to further suppress HFR in the MMC-HVDC system, an enhanced impedance reshaping control strategy based on the equivalent single-input single-output impedance model is proposed. Finally, the accuracy of the enhanced impedance model and the effectiveness of the impedance reshaping control are verified by electromagnetic transient simulations in PSCAD.**

***Index Terms*—Modular multilevel converter based high-voltage direct current (MMC-HVDC), high-frequency resonance, frequency coupling, impedance model, impedance reshaping control.**

I. Introduction

MODULAR multilevel converter based high-voltage direct current (MMC-HVDC) transmission has been widely used in renewable energy systems, large-scale and long-distance power transmissions, and asynchronous network interconnections [1]-[4]. Nevertheless, sub-synchronous resonance at 10-30 Hz, medium-frequency resonance at 250-350 Hz, and high-frequency resonance (HFR) at 550-3000 Hz have been observed in several practical high-voltage direct current (HVDC) projects. HFR phenomena are generally caused by the interaction between modular multilevel converter (MMC) and alternating current (AC) systems [5]-[8]. A 1.6 kHz HFR event was reported in the INELFE project [5], and similar HFR events also occurred in both the Luxi [6] and Chongqing-Hubei back-to-back HVDC projects in China [7]. These HFRs can distort the AC system and result in large fluctuations in voltages and currents.

Currently, sub- or super-synchronous resonances or HFRs in power systems are primarily analyzed by using the eigenvalue-based method [9]-[13] or impedance-based method [14]-[18]. The eigenvalue-based method can present system eigenvalues and reveal their stability using the state-space model [9]-[13]. However, the impedance-based method focuses on the port characteristics of an MMC-HVDC system, in which the system is divided into two sub-systems, namely, MMC and AC. The Nyquist stability criterion is usually used to assess stability with sub-system impedances [14] and states that a resonance will occur when the phase angle difference is greater than 180° at the amplitude intersection of the MMC and AC system impedances [5]. Therefore, HFR usually occurs in the frequency band in which the MMC impedance phase is greater than 90°. In other words, MMC impedance presents inductive negative damping characteristics [15].

In [5], a simplified MMC impedance model is established for HFR analysis. The paper indicates that the time delay of the MMC is the main reason for the negative damping characteristics of the MMC impedance and that the risk of HFR could be lowered by reducing the time delay. To suppress the negative damping characteristics, a low-pass filter (LPF) in the voltage feed-forward path is presented in [6]. However, the impedance characteristics at medium frequencies may deteriorate via this path. A novel nonlinear filter is proposed in [7] to filter out harmonic components in the voltage feed-forward path, presenting a better harmonic suppression effect than the LPF in [6].

In addition, an HFR damping controller is proposed in [16], in which the AC voltage is superimposed with the ref-

Manuscript received: October 26, 2022; revised: February 12, 2023; accepted: June 9, 2023. Date of CrossCheck: June 9, 2023. Date of online publication: August 24, 2023.

This work was supported by National Natural Science Foundation of China (No. 52277102).

J. Wang, W. Chen (corresponding author), and Y. Liu are with the School of Electric Power, South China University of Technology, Guangzhou, China, and W. Chen is also with Guangdong Power Grid Co., Ltd., Guangzhou, China (e-mail: epjjwang@scut.edu.cn; 490782425@qq.com; yuekunliu@qq.com).

C. Fu and J. Feng are with the Electric Power Research Institute, China Southern Power Grid, Guangzhou, China (e-mail: fuchuang@csg. cn; junjiefeng@csg.cn).

Y. Ye is with Guangdong Power Grid Co., Ltd., Guangzhou, China (e-mail: 1151321986@qq.com).

DOI: 10.35833/MPCE.2022.000702

erence current after passing through the damping controller. However, the damping controller design is quite complicated because its order is high. Reference [17] shows that the phase-locked loop (PLL) has a negligible influence on impedance characteristics at high frequencies, and the negative damping characteristics of MMC can be reduced by the proportional coefficient of current and power loops. A new passive damper for MMCs that considers arm inductors is proposed in [18]. Finally, a novel HFR suppression measure is proposed in [15], which is achieved by adding an LPF to the voltage feed-forward path and an LPF to the proportional path of the current control.

Nevertheless, in the aforementioned studies, the MMC is regarded as a single-input single-output (SISO) system, and the frequency coupling effect of the MMC is not considered, which may lead to an inaccurate impedance model and stability analytical results [19]. In general, if a perturbation voltage with frequency f_{P1} is injected into the point of common coupling (PCC), corresponding currents will exist at frequencies f_{P1} and $2f_1-f_{\mathrm{P1}}$ at the PCC [20]. The coupling current at frequency $2f_1-f_{\mathrm{P1}}$ will generate a perturbation voltage at the same frequency through the AC system impedance and in turn lead to further coupling with the perturbation current at frequency f_{P1}. Therefore, MMC-HVDC systems present multi-input multi-output (MIMO) characteristics [21]. Because of their asymmetry in the *dq* frame, the current control and PLL are the main reasons for these MIMO characteristics [22]-[24].

Frequency coupling occurs in interconnected systems with AC/DC power electronic equipment such as MMC-HVDCs, three-phase grid-connected inverters, and doubly-fed induction generator (DFIG) systems. The mechanism of frequency coupling can be analyzed using a similar method. A two-dimensional MIMO admittance matrix is proposed to describe the port characteristics of the MMC system and is then decomposed by a novel method into an SISO system for stability analysis [23]. In SISO systems, the Nyquist criterion is more convenient for stability analysis than the generalized Nyquist criterion (GNC) in MIMO systems [24]. For a photovoltaic inverter connected to an AC grid, the frequency coupling increases with a decreasing short-circuit ratio (SCR) of the AC grid, and its impact on system stability is greater [25]. When a DFIG system adopts direct power control, the time delay can intensify the frequency coupling degree, leading to periodic changes in the equivalent impedance phase at high frequencies, which indicates that the time delay and frequency coupling will affect system stability [26], [27]. In general, the time delay of MMC-HVDC systems can reach 400-500 μs, which is greater than that of grid-connected inverters or DFIG systems [6], [7]. However, an analytical frequency coupling impedance model suitable for analyzing HFR in MMC-HVDC systems and the effects of time delay and frequency coupling on system stability must be further studied.

Accordingly, in this paper, an MIMO admittance model of an MMC-HVDC system is developed. The effects of time delay on impedance characteristics and those of the PLL, current loop, power loop, and SCR on the MMC frequency coupling degree are analyzed. Focusing on the significant frequency coupling effect in the high-frequency band, this paper proposes a frequency coupling suppression method that considers the power loop. An improved control method is also offered to suppress the HFR with a flexible control parameter adaptive to the negative damping frequency band of the MMC. The effectiveness of the improved control method is verified via the electromagnetic transient (EMT) model of the Luxi back-to-back HVDC project.

The rest of this paper is organized as follows. Section II introduces the control structure of MMC-HVDC system. Section III introduces frequency coupling model of MMC-HVDC system. Section IV describes the establishment of frequency coupling admittance model of the MMC-HVDC system. Section V presents the stability analysis based on frequency coupling impedance model. Section VI analyzes the novel HFR suppression strategy based on the impedance reshaping control strategy. Section VII concludes the paper.

II. Control Structure of MMC-HVDC System

This paper focuses on the impedance characteristics of the MMC-HVDC system at medium and high frequencies. Because the control mainly affects the impedance characteristics of MMC in the low-frequency bands, the following can be ignored: ① circulating current suppression control (CCSC) [13], ② capacitor voltage balancing algorithm, and ③ dynamics of the bridge arm [28].

The equivalent circuit at the inverter side of the MMC-HVDC system is shown in Fig. 1, where Z_{g} is the system impedance; and V_{g} is the AC system voltage.

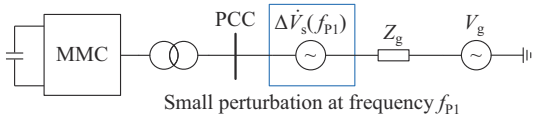

Fig. 1. Equivalent circuit at inverter side of MMC-HVDC system.

The control circuit of MMC is shown in Fig. 2, in which a dual closed-loop control structure is adopted. The power loop achieves constant active and reactive power controls, and the current loop independently controls the positive- and negative-sequence currents [3].

In Fig. 2, $u_{d\mathrm{P}}$, $u_{q\mathrm{P}}$ and $u_{d\mathrm{N}}$, $u_{q\mathrm{N}}$ are the positive- and negative-sequence *dq*-axis components of AC voltage u_{ABC}, respectively; $i_{d\mathrm{P}}$, $i_{q\mathrm{P}}$ and $i_{d\mathrm{N}}$, $i_{q\mathrm{N}}$ are the positive- and negative-sequence *dq*-axis components of AC current i_{ABC}, respectively; θ_{PLL} is the positive-sequence phase angle output by PLL; G_{sd} is the transfer function (TF) of the quarter fundamental frequency periodic delay filter; P, P^{ref}, Q, and Q^{ref} are the active power, active power reference, reactive power, and reactive power reference, respectively; $i_{d\mathrm{P}}^{\mathrm{ref}}$ and $i_{q\mathrm{P}}^{\mathrm{ref}}$ are the references of *dq*-axis current; G_{PQ} and G_{i} are the proportional integra (PI) controllers of the power and current control, respectively; K_{d} is the decoupling coefficient of the current inner loop; G_{f} is the TF of the second-order LPF in the voltage feed-forward path; G_{d} is the system delay; $u_{d\mathrm{P}}^{\mathrm{ref}}$, $u_{q\mathrm{P}}^{\mathrm{ref}}$ and $u_{d\mathrm{N}}^{\mathrm{ref}}$, $u_{q\mathrm{N}}^{\mathrm{ref}}$ are the *dq*-axis components of the voltage reference from the positive- and negative-sequence current inner loops,

respectively; $u_{\mathrm{ABCP}}^{\mathrm{ref}}$ and $u_{\mathrm{ABCN}}^{\mathrm{ref}}$ are the positive- and negative-sequence voltage references, respectively; and $u_{\mathrm{ABC}}^{\mathrm{ref}}$ is the voltage reference in three-phase frame.

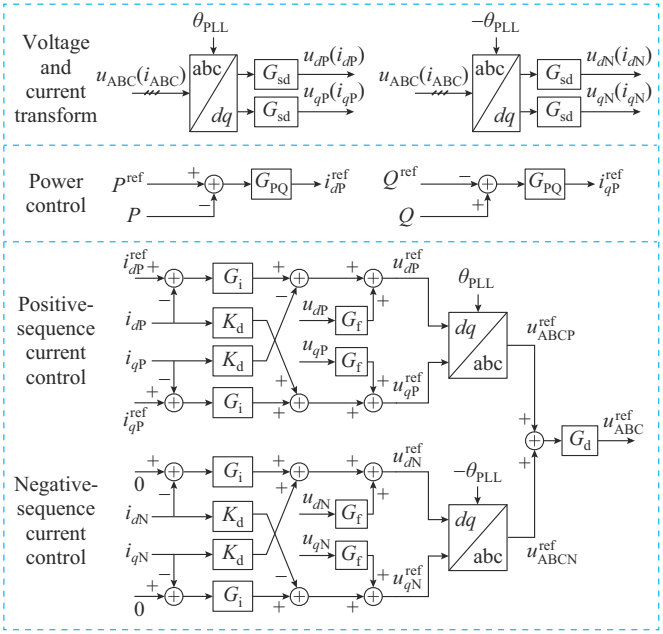

Fig. 2. Control circuit of MMC.

Figure 3 shows the schematic of control link delay composition of a practical MMC control system, which consists of voltage and current transformers, an analog-to-digital conversion (ADC) unit, converter control, valve base control, submodule (SM) control, and zero-order holder (ZOH) equivalent delay. The link delay of the entire control system can be represented by a lumped delay T_{d} in series with the ZOH equivalent delay T_{s}. Then, G_{d} can be expressed as:

$$G_{\mathrm{d}}(f)=\mathrm{e}^{-\mathrm{j}2\pi fT_{\mathrm{d}}}(1-\mathrm{e}^{-\mathrm{j}2\pi fT_{\mathrm{s}}})/(\mathrm{j}2\pi fT_{\mathrm{s}}) \tag{1}$$

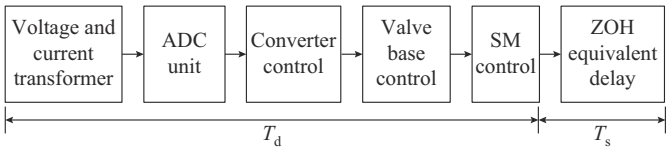

Fig. 3. Schematic of control link delay composition of a practical MMC control system.

III. Frequency Coupling Model of MMC-HVDC System

A. Definition of MIMO Admittance Model of MMC

Assuming that a small perturbation voltage at frequency f_{P1} ($\Delta\dot{V}_{\mathrm{s}}(f_{\mathrm{P1}})$) is injected into the AC system, as shown in Fig. 1, the PCC will contain perturbation components both at frequency f_{P1} and coupling frequency $2f_1-f_{\mathrm{P1}}$. Let $f_{\mathrm{P2}}=2f_1-f_{\mathrm{P1}}$. The voltage and current of phase A at PCC can be expressed as:

$$\begin{cases} v_{\mathrm{A}}=V_1\cos(\omega_1 t)+V_{\mathrm{P1}}\cos(\omega_{\mathrm{P1}}t+\varphi_{\mathrm{P1}})+V_{\mathrm{P2}}\cos(\omega_{\mathrm{P2}}t+\varphi_{\mathrm{P2}}) \\ i_{\mathrm{A}}=I_1\cos(\omega_1 t+\varphi_{\mathrm{i1}})+I_{\mathrm{P1}}\cos(\omega_{\mathrm{P1}}t+\varphi_{\mathrm{iP1}})+I_{\mathrm{P2}}\cos(\omega_{\mathrm{P2}}t+\varphi_{\mathrm{iP2}}) \end{cases} \tag{2}$$

where V_1 and ω_1 are the amplitude and angular frequency of the fundamental frequency voltage, respectively; V_{P1} and φ_{P1} are the amplitude and phase of the perturbation voltage at ω_{P1}, respectively; V_{P2} and φ_{P2} are the amplitude and phase of the perturbation voltage at ω_{P2}, respectively; I_1 and φ_{i1} are the fundamental frequency amplitude and phase of the current, respectively; I_{P1} and φ_{iP1} are the amplitude and phase of the perturbation current at ω_{P1}, respectively; and I_{P2} and φ_{iP2} are the amplitude and phase of the perturbation current at ω_{P2}, respectively.

Let $\dot{I}_{\mathrm{P1}}=0.5I_{\mathrm{P1}}\mathrm{e}^{\mathrm{j}\varphi_{\mathrm{iP1}}}$, $\dot{I}_{\mathrm{P2}}=0.5I_{\mathrm{P2}}\mathrm{e}^{\mathrm{j}\varphi_{\mathrm{iP2}}}$, $\dot{V}_{\mathrm{P1}}=0.5V_{\mathrm{P1}}\mathrm{e}^{\mathrm{j}\varphi_{\mathrm{P1}}}$, and $\dot{V}_{\mathrm{P2}}=0.5V_{\mathrm{P2}}\mathrm{e}^{\mathrm{j}\varphi_{\mathrm{P2}}}$. The MIMO admittance model of MMC can then be described by a 2×2 matrix $\boldsymbol{Y}_{\mathrm{MMC}}$ as:

$$\begin{bmatrix}\dot{I}_{\mathrm{P1}}\\ \dot{I}_{\mathrm{P2}}^*\end{bmatrix}=\underbrace{\begin{bmatrix}Y_{11}&Y_{12}\\ Y_{21}&Y_{22}\end{bmatrix}}_{\boldsymbol{Y}_{\mathrm{MMC}}}\begin{bmatrix}\dot{V}_{\mathrm{P1}}\\ \dot{V}_{\mathrm{P2}}^*\end{bmatrix} \tag{3}$$

where the diagonal elements Y_{11} and Y_{22} represent self-admittances; the non-diagonal elements Y_{12} and Y_{21} represent coupling admittances; and the superscript * indicates a conjugate operation.

According to [29], $\boldsymbol{Y}_{\mathrm{MMC}}$ has the following symmetric characteristics:

$$\begin{cases} Y_{11}(f_{\mathrm{P1}})=Y_{22}(2f_1-f_{\mathrm{P1}})^* \\ Y_{21}(f_{\mathrm{P1}})=Y_{12}(2f_1-f_{\mathrm{P1}})^* \end{cases} \tag{4}$$

Therefore, the frequency coupling effect can be analyzed based on Y_{11} and Y_{21}. In addition, when the amplitudes of the coupling admittance are sufficiently small, their effects on system stability can be ignored. Accordingly, the impedance matrix can be expressed as:

$$\begin{bmatrix}\dot{V}_{\mathrm{p1}}\\ \dot{V}_{\mathrm{p2}}^*\end{bmatrix}=\begin{bmatrix}Z_{11}&0\\ 0&Z_{22}\end{bmatrix}\begin{bmatrix}\dot{I}_{\mathrm{p1}}\\ \dot{I}_{\mathrm{p2}}^*\end{bmatrix} \tag{5}$$

where $Z_{11}=1/Y_{11}$ and $Z_{22}=1/Y_{22}$.

B. Equivalent SISO Impedance Model of MMC

The AC system can be described in the frequency domain as:

$$\begin{cases} \dot{V}_{\mathrm{P1}}=\dot{V}_{\mathrm{s}}(f_{\mathrm{P1}})-\dot{I}_{\mathrm{P1}}Z_{\mathrm{g}}(f_{\mathrm{P1}}) \\ \dot{V}_{\mathrm{P2}}^*=-\dot{I}_{\mathrm{P2}}^*Z_{\mathrm{g}}^*(2f_1-f_{\mathrm{P1}}) \end{cases} \tag{6}$$

Based on (3) and (6), the MIMO admittance model of MMC-HVDC system is shown in Fig. 4. The equivalent SISO impedance model can be obtained, and Y_{eq} can be expressed as:

$$\begin{cases} Y_{\mathrm{eq}}=\dfrac{\dot{I}_{\mathrm{P1}}}{\dot{V}_{\mathrm{P1}}}=Y_{11}-Y_{\mathrm{con}} \\ Y_{\mathrm{con}}=\dfrac{Y_{12}Y_{21}Z_{\mathrm{g}}^*(2f_1-f_{\mathrm{p1}})}{1+Y_{22}Z_{\mathrm{g}}^*(2f_1-f_{\mathrm{p1}})} \end{cases} \tag{7}$$

where Y_{con} is the admittance introduced by frequency coupling characteristics that contain MMC system admittance and coupling impedance $Z_{\mathrm{g}}^*(2f_1-f_{\mathrm{P1}})$.

The equivalent SISO impedance can be expressed as $Z_{\mathrm{eq}}=1/Y_{\mathrm{eq}}$.

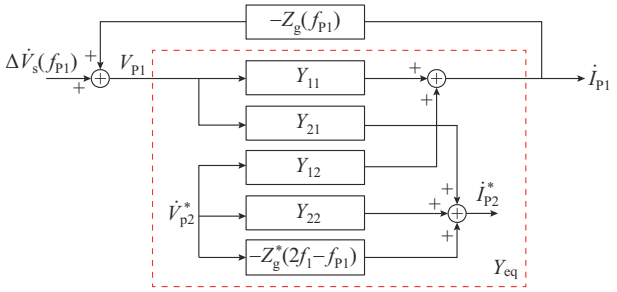

Fig. 4. MIMO admittance model of MMC-HVDC system.

The larger the amplitude of Y_{con}, the greater the effect of the frequency coupling on Y_{eq}, and vice versa. When the amplitude of Y_{con} is sufficiently small, Y_{con} has a negligible influence, and then $Y_{eq} \approx Y_{11}$.

IV. Establishment of Frequency Coupling Admittance Model of MMC-HVDC

A. MIMO Admittance Model of MMC

1) PLL

The closed-loop TF of the PLL is expressed as:

$$\begin{cases} G_{PLL}(f) = H_{PLL}(f)/[1 + V_1 H_{PLL}(f)] \\ H_{PLL}(f) = (K_{p,PLL} + K_{i,PLL}/(j2\pi f))/(j2\pi f) \end{cases} \tag{8}$$

where $K_{p,PLL}$ and $K_{i,PLL}$ are the PI parameters of the PLL. The output phase angle of PLL can be obtained by:

$$\Delta\theta(f) = \begin{cases} -jG_{PLL}(f)(\dot{V}_{p1} - \dot{V}^*_{p2}) & f = f_{p1} - f_1 \\ jG_{PLL}(f)(\dot{V}^*_{p1} - \dot{V}_{p2}) & f = f_1 - f_{p1} \end{cases} \tag{9}$$

Note that $\Delta\theta(f_1 - f_{p1}) = (\Delta\theta(f_{p1} - f_1))^*$; that is, the expression of $\Delta\theta(f)$ at $f = f_{p1} - f_1$ and $f = f_1 - f_{p1}$ has the following symmetrical relationship: $G(j2\pi f) = (G(-j2\pi f))^*$. This symmetrical relationship is applicable to other electrical quantities. To simplify the equation, only the expression of the electrical quantity at f is given, and the expression at $-f$ can be obtained based on the symmetrical relationship.

2) Power Loop

The active and reactive power perturbations can be obtained in the frequency domain by:

$$\begin{cases} \Delta P(f) = (\dot{V}^*_1 \dot{I}_{p1} + \dot{V}_{p1} \dot{I}^*_1 + \dot{V}_1 \dot{I}^*_{p2} + \dot{V}^*_{p2} \dot{I}_1) & f = f_{P1} - f_1 \\ \Delta Q(f) = j(\dot{V}^*_1 \dot{I}_{p1} - \dot{V}_{p1} \dot{I}^*_1 - \dot{V}_1 \dot{I}^*_{p2} + \dot{V}^*_{p2} \dot{I}_1) & f = f_{P1} - f_1 \end{cases} \tag{10}$$

According to Fig. 2, the reference current perturbations can be expressed as:

$$\begin{cases} \Delta i^{ref}_{dP}(f) = -G_{PQ}(f)\Delta P(f) \\ \Delta i^{ref}_{qP}(f) = G_{PQ}(f)\Delta Q(f) \end{cases} \tag{11}$$

3) Positive- and Negative-sequence Current Loops

The voltage and current perturbations in the positive-sequence dq frame at $f = f_{p1} - f_1$ can be expressed as:

$$\Delta u_{dP}(f) = G_{sd}(f)(\dot{V}_{p1} + \dot{V}^*_{p2}) \quad f = f_{p1} - f_1 \tag{12a}$$

$$\Delta u_{qP}(f) = -jG_{sd}(f)(\dot{V}_{p1} - \dot{V}^*_{p2}) - G_{sd}(f)V_1\Delta\theta(f) \quad f = f_{P1} - f_1 \tag{12b}$$

$$\Delta i_{dP}(f) = G_{sd}(f)(\dot{I}_{p1} + \dot{I}^*_{p2}) \quad f = f_{p1} - f_1 \tag{12c}$$

$$\Delta i_{qP}(f) = -jG_{sd}(f)(\dot{I}_{p1} - \dot{I}^*_{p2}) - V_1 G_{sd}(f)\Delta\theta(f) \quad f = f_{P1} - f_1 \tag{12d}$$

where G_{sd} is expressed as:

$$G_{sd}(f) = 0.5(1 + e^{-j2\pi fT/4}) \tag{13}$$

where T is the fundamental frequency period.

Similarly, the expressions for perturbations in the negative-sequence current loop, i.e., Δu_{dN}, Δu_{qN}, Δi_{dN}, and Δi_{qN}, can be obtained. The derivation process is found in [17].

According to Fig. 2, the perturbation in the reference voltages in the dq frame can be obtained by:

$$\begin{cases} \Delta u^{ref}_{dP}(f) = -G_i(f)(\Delta i^{ref}_{dP}(f) - \Delta i_{dP}(f)) + \\ \qquad G_f(f)\Delta u_{dP}(f) + K_d\Delta i_{qP}(f) \\ \Delta u^{ref}_{qP}(f) = -G_i(f)(\Delta i^{ref}_{qP}(f) - \Delta i_{qP}(f)) + \\ \qquad G_f(f)\Delta u_{qP}(f) - K_d\Delta i_{dP}(f) \end{cases} \tag{14}$$

$$\begin{cases} \Delta u^{ref}_{dN}(f) = G_i(f)\Delta i_{dN}(f) - K_d\Delta i_{qN}(f) + G_f(f)\Delta u_{dN}(f) \\ \Delta u^{ref}_{qN}(f) = G_i(f)\Delta i_{qN}(f) + K_d\Delta i_{dN}(f) + G_f(f)\Delta u_{qN}(f) \end{cases} \tag{15}$$

The second-order LPF is expressed as:

$$G_f(f) = \frac{\omega^2_{LPF}}{(j2\pi f)^2 + 2\xi\omega_{LPF}(j2\pi f) + \omega^2_{LPF}} \tag{16}$$

where ζ is the damping ratio, the value of which is 0.707; and ω_{LPF} is the cutoff frequency of the LPF.

The positive- and negative-sequence voltage references can be obtained by:

$$\begin{cases} u^{ref}_{AP} = F(\cos(\omega_1 t) - \Delta\theta\sin(\omega_1 t))F(u^{ref}_{dP}(t)) + \\ \qquad F(-\sin(\omega_1 t) - \Delta\theta\cos(\omega_1 t))F(u^{ref}_{qP}(t)) \\ u^{ref}_{AN} = F(\cos(\omega_1 t) - \Delta\theta\sin(\omega_1 t))F(u^{ref}_{dN}(t)) - \\ \qquad F(-\sin(\omega_1 t) - \Delta\theta\cos(\omega_1 t))F(u^{ref}_{qN}(t)) \end{cases} \tag{17}$$

where $F(y(t))$ is the frequency-domain transformation of the time-domain signal $y(t)$. The frequency-domain expression of perturbations in u^{ref}_{AP} is given by:

$$\Delta u^{ref}_{AP}(f) = \begin{cases} \frac{1}{2}\Delta u^{ref}_{dP}(f - f_1) + \frac{j}{2}\Delta u^{ref}_{qP}(f - f_1) + \\ \qquad \left(\frac{j}{2}u^{ref}_{dP0} - \frac{1}{2}u^{ref}_{qP0}\right)\Delta\theta(f - f_1) & f = f_{P1} \\ \frac{1}{2}\Delta u^{ref}_{dP}(f + f_1) + \frac{j}{2}\Delta u^{ref}_{qP}(f + f_1) - \\ \qquad \left(\frac{j}{2}u^{ref}_{dP0} + \frac{1}{2}u^{ref}_{qP0}\right)\Delta\theta(f + f_1) & f = f_{P1} - 2f_1 \end{cases} \tag{18}$$

where u^{ref}_{dP0} and u^{ref}_{qP0} are the steady-state quantities of the positive-sequence dq-axis reference voltage, respectively. Similarly, the expression of Δu^{ref}_{AN} can be obtained.

4) Frequency Coupling Impedance Model of MMC

The perturbations of output voltage of phase A can be expressed as:

$$\Delta u^{out}_A(f) = G_d(f)(\Delta u^{ref}_{AP}(f) + \Delta u^{ref}_{AN}(f)) \tag{19}$$

According to the AC equivalent circuit, the AC-side dynamic equations can be obtained by:

$$\begin{cases}\dot{V}_{p1}-\Delta u_A^{out}(f_{p1})=j2\pi f_{p1}L\dot{I}_{p1}\\ \dot{V}_{p2}-\Delta u_A^{out}(2f_1-f_{p1})=j2\pi(2f_1-f_{p1})L\dot{I}_{p2}\end{cases} \tag{20}$$

where L is the equivalent inductance on the AC side of the converter.

Based on (8)-(20), the admittance matrix $\boldsymbol{Y}_{MMC}$ can be derived. As the PLL control can be ignored, $\boldsymbol{Y}_{MMC}$ can be simplified and derived by the following equation, in which Y_{21} and Y_{22} are not given due to page limitation.

$$\begin{cases}Y_{11}=\dfrac{1-G_d(s)[G_f(s-s_1)G_{sd}(s-s_1)+G_f(s+s_1)G_{sd}(s+s_1)]}{sL+G_d(s)[G_i(s-s_1)G_{sd}(s-s_1)+G_i(s+s_1)G_{sd}(s+s_1)-jK_dG_{sd}(s-s_1)+jK_dG_{sd}(s+s_1)+A(s)]}\\ Y_{21}=\dfrac{-G_d(s-2s_1)G_i(s-s_1)G_{PQ}(s-s_1)I_1}{(s-2s_1)L+G_d(s-2s_1)[G_i(s-s_1)G_{sd}(s-s_1)+G_i(s-3s_1)G_{sd}(s-3s_1)-jK_dG_{sd}(s-3s_1)+jK_dG_{sd}(2s_1-s)+A(s)]}\end{cases} \tag{21}$$

where $A(s)=G_i(s-s_1)G_{PQ}(s-s_1)V_1$; $s=j2\pi f$; and $s_1=j2\pi f_1$.

B. Verification of MIMO Admittance Model

The MIMO admittance model of MMC is established in MATLAB. The EMT model is established in PSCAD, which is the same as the inverter of the Luxi back-to-back HVDC project in China. The parameters of the MMC-HVDC system and MMC controllers are shown in Tables I and II, respectively. The structure and parameters of the AC system are the same as those given in [6], which are presented in Fig. 5 and Table I, respectively.

TABLE I
PARAMETERS OF MMC-HVDC SYSTEM

Category	Parameter	Value
MMC	Rated capacity (MVA)	1000
	Primary voltage (kV)	525
	Rated DC voltage (kV)	700
	Arm inductor (mH)	104
	T_d (μs)	400
	T_s (μs)	100
Transformer	Rated capacity (MVA)	1000
	Transformation ratio	525/375
	Leakage inductance (%)	14
AC system	L_g (mH)	169.3
	C_g (uF)	0.18
	R_1 (Ω)	8.4
	R_2 (Ω)	171

TABLE II
PARAMETERS OF MMC CONTROLLERS

Parameter	Value
Proportional/integral coefficient of PLL	0.01/0.04
Proportional/integral coefficient of current controller	1.0/10
Proportional/integral coefficient of power controller	0.8/20

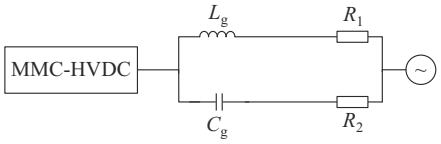

Fig. 5. Structure of AC system.

To verify the correctness of $\boldsymbol{Y}_{MMC}$, the impedance scanning method is adopted in the EMT model. A controlled voltage source is used to superimpose a perturbation voltage with an amplitude of 5 kV on the grid voltage, and its frequency range is 10-3000 Hz. The scanning frequency interval is 100 Hz. Figure 6 shows the frequency characteristics of MIMO admittance. The calculation results in MATLAB and the simulation results in PSCAD are consistent.

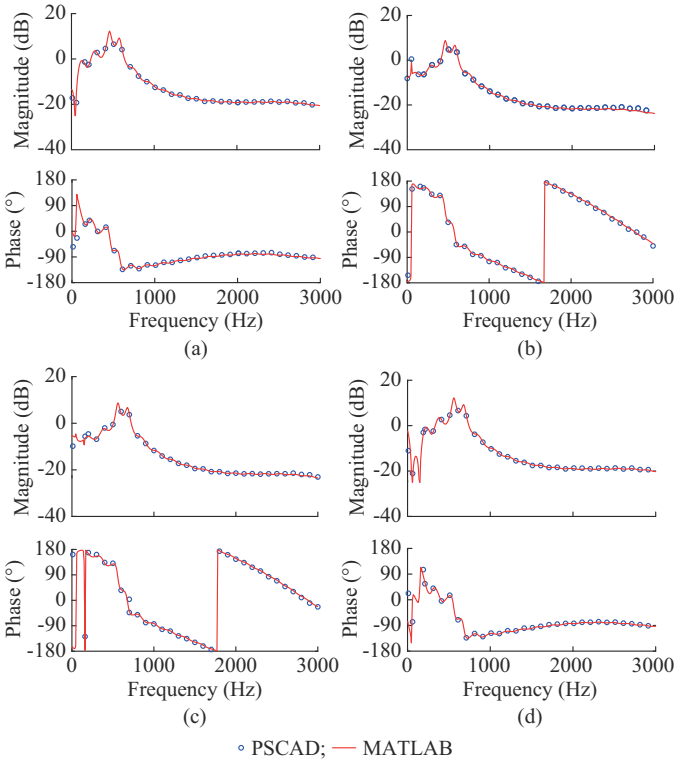

Fig. 6. Frequency characteristics of MIMO admittance. (a) Y_{11}. (b) Y_{12}. (c) Y_{21}. (d) Y_{22}.

V. STABILITY ANALYSIS BASED ON FREQUENCY COUPLING IMPEDANCE MODEL

A. Frequency Characteristic Analysis of Self-impedance Z_{11}

The frequency characteristics of the self-impedance have been analyzed in detail in [17]. The delay time of the control system and the voltage feed-forward path have significant effects on the impedance characteristics of Z_{11}.

When the second-order LPF in the voltage feed-forward path is not considered, i. e., $G_f=1$, the effects of different lumped delays on the impedance characteristics of Z_{11} can be illustrated, as shown in Fig. 7.

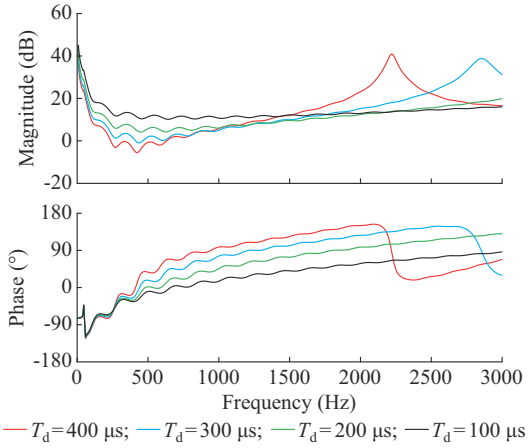

Fig. 7. Impedance characteristics of Z_{11} under different delays.

When T_d is 100 μs, the phase of the MMC impedance is less than 90°. With an increase in T_d, the phase of the MMC impedance is greater than 90° in the high-frequency band, showing more obvious negative damping characteristics, which is the main reason for the HFR. As Fig. 8 shows, after the second-order LPF in the voltage feed-forward path is adopted, the impedance characteristics at high frequencies can be improved. However, the impedance characteristics at middle frequencies deteriorate and show more obvious negative damping characteristics. In addition, reducing the bandwidth of the LPF, i.e., 100 Hz, cannot prevent deterioration.

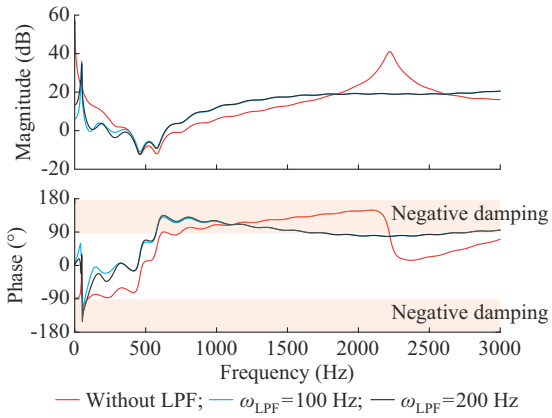

Fig. 8. Impedance characteristics of MMC with LPF inserted in voltage feed-forward path.

Figure 9 shows the impedance characteristics of Z_{11} before and after considering PLL. The impedance characteristics of MMC remain essentially unchanged because the TF of the PLL has a strong attenuation in the frequency band (except at approximately 50 Hz), and therefore, the effect of the PLL can be ignored when HFR is analyzed. Thus, the simplification of (21) is reasonable.

B. Frequency Coupling Degree Analysis

Based on the analysis presented in Section III, the frequency coupling degree is related to the amplitude of the diagonal and non-diagonal elements of the admittance matrix $\boldsymbol{Y}_{MMC}$.

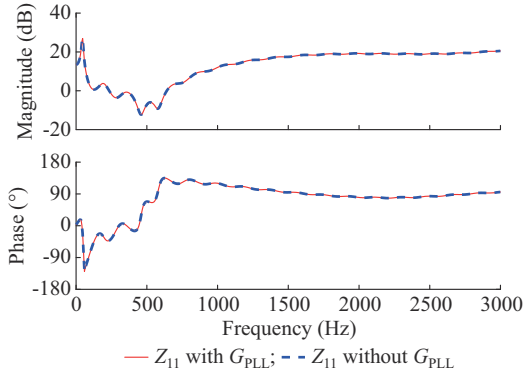

Fig. 9. Impedance characteristics of Z_{11} before and after considering PLL.

When the symmetry of the admittance matrix is considered, a frequency coupling coefficient (FCC) is defined by the following equation to describe the frequency coupling degree qualitatively. The smaller the FCC, the smaller the frequency coupling, and vice versa.

$$FCC = 20\lg\frac{|Y_{21}|}{|Y_{11}|} \tag{22}$$

Figure 10(a) and (b) shows the effects of the current loop proportional coefficient $K_{p,i}$ and power loop proportional coefficient $K_{p,pq}$ on the FCC. Clearly, FCC decreases with a decrease in $K_{p,i}$ or $K_{p,pq}$, and thus the frequency coupling degree also decreases.

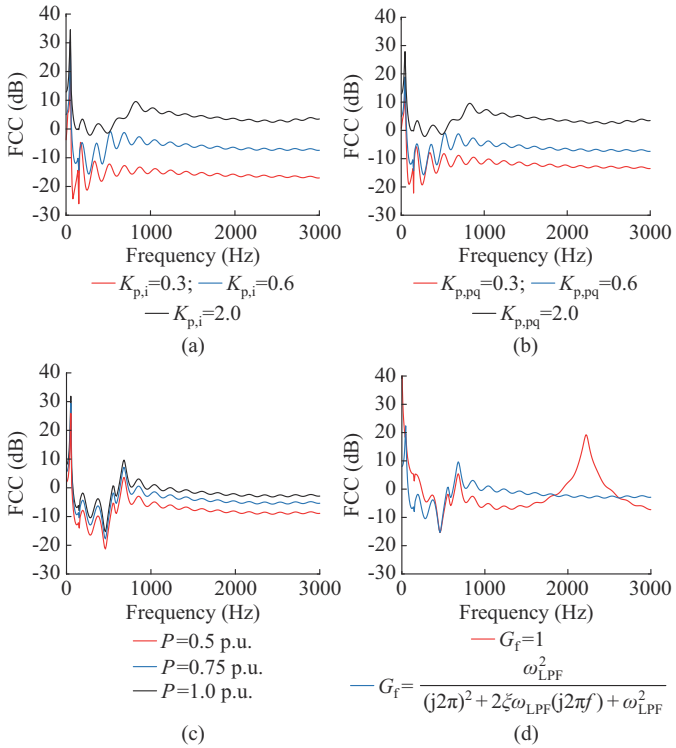

Fig. 10. FCC curves under different parameters. (a) $K_{p,i}$. (b) $K_{p,pq}$. (c) DC power. (d) G_f.

The impedance model is obtained by linearizing the nonlinear model at the operating point. Therefore, analyzing the effects of the operating point on the frequency coupling ef-

fect is necessary. Figure 10(c) shows the FCC curves when the DC power is 1.0 p.u., 0.75 p.u., and 0.5 p.u., respectively. FCC decreases with DC power, and thus, the frequency coupling degree also decreases. It should be noted that Y_{11} in (21) and Y_{22} are independent of I_1. Therefore, different steady-state operating points under a unity power factor have no effect on the impedance characteristics of Y_{11} and Y_{22}. However, Y_{12} and Y_{21} have a linear relationship with I_1. Thus, when the operating point changes, only the impedance characteristics of Y_{12} and Y_{21} are affected.

Figure 10(d) shows the effects of the voltage feed-forward path on the FCC. According to (21), the expression of Y_{21} does not include G_f inserted in the voltage feed-forward path, and therefore, the LPF does not help to improve the frequency characteristics of Y_{21}. Thus, after the second-order LPF is adopted, the FCC does not decrease significantly in the high-frequency band.

Figure 11 shows the FCC curves under different PLL bandwidths. The effects of PLL bandwidth on the FCC curve are mainly less than 150 Hz when the PLL bandwidth changes from 10 to 30 Hz, and the frequency characteristics in the high-frequency band are basically the same. Therefore, although the PLL is a major reason for the frequency coupling effect [22], it has little influence on the frequency coupling effect of MMC in the high-frequency band.

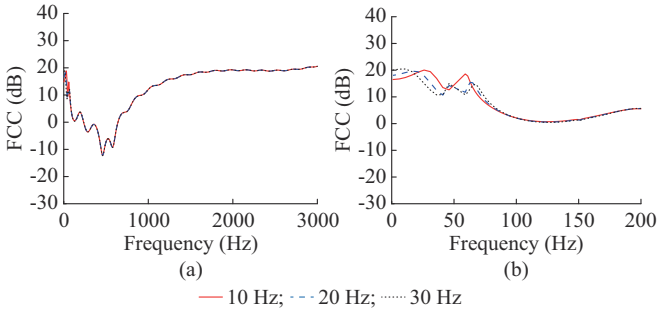

Fig. 11. FCC curves under different PLL bandwidths. (a) Frequency ranging from 0 to 3000 Hz. (b) Frequency ranging from 0 to 200 Hz.

C. Improved Frequency Coupling Suppression Method (FCSM) to Reduce Frequency Coupling Degree

Next, an improved FCSM is proposed to reduce the frequency coupling degree. Because the coupling voltage and current components are mainly transmitted to the control system of the MMC through the power calculation path, a first-order LPF can be inserted into the power calculation path to filter out the high-frequency components.

The FCC curves under different T_{LPF} are shown in Fig. 12, where T_{LPF} is the time constant of an LPF. With the increase in T_{LPF} from 2 to 10 ms, the FCC decreases significantly, and the frequency coupling degree also decreases. Because of the fast dynamic response performance of the system, T_{LPF} can be set to be 5 ms. In this case, the impedance characteristics of Z_{11} and Z_{eq} with the FCSM are essentially the same, as shown in Fig. 13, which proves the effectiveness of the FCSM.

Figure 13 shows the impedance characteristics of MMC and AC systems.

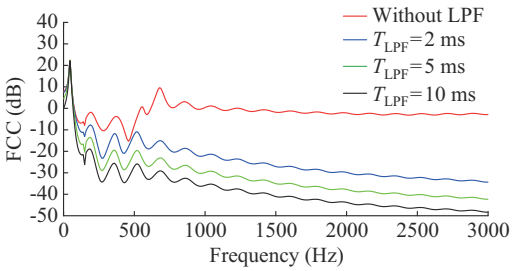

Fig. 12. FCC curves under different T_{LPF}.

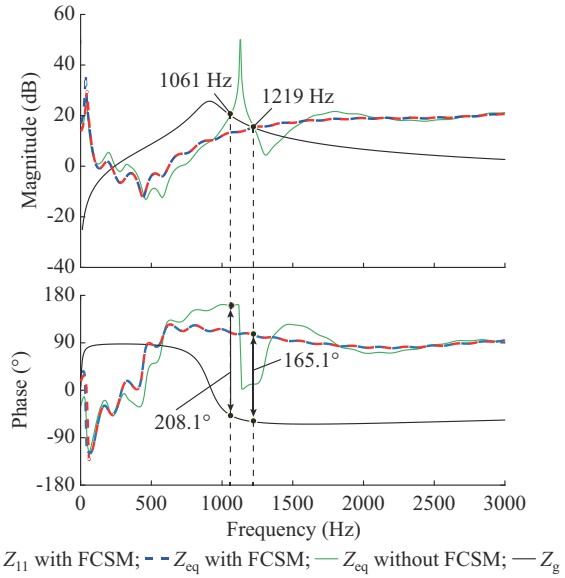

Fig. 13. Impedance characteristics of MMC and AC systems.

When FCSM is not adopted, the impedance characteristics of Z_{eq} show obvious negative damping in the high-frequency band. The phase angle difference is greater than 180° at the cutoff frequency of 1061 Hz, and therefore, the system cannot maintain stability. When the LPF (T_{LPF} = 5 ms) is added to the power loop, the phase difference between Z_{eq} and Z_g is 165.1° at a cutoff frequency of 1219 Hz. Therefore, the system remains stable.

The negative-damping characteristics of MMC impedance mainly derive from the system link delay, which is the main reason for the HFR. The frequency coupling effect increases the complexity of the system analysis, and if it is not considered, it may lead to incorrect stability analytical results.

To further verify the correctness of the aforementioned analysis, a simulation is conducted in the EMT model, as shown in Fig. 14. The lumped delay T_d increases from 0 to 400 μs at 1.0 s, and then the FCSM is adopted at 1.2 s.

Two instances of HFR clearly occur in the system, and the resonant frequencies are 1060 Hz and 960 Hz, respectively, where the difference of 100 Hz satisfies the frequency coupling relationship, indicating that the MMC-HVDC system has strong frequency coupling characteristics. The resonance frequency is basically the same as the analytical result presented in Fig. 13, thus verifying the theoretical analysis. When the LPF is placed into operation, the system gradually returns to stability, thus verifying the effectiveness of the proposed FCSM.

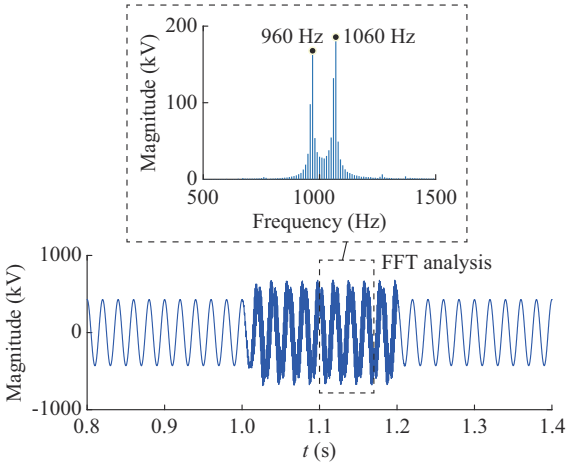

Fig. 14. Phase A voltage from PCC and FFT analytical results.

VI. Novel HFR Suppression Strategy Based on Impedance Reshaping Control Strategy

Although the frequency coupling degree can be reduced by adopting the method proposed in the previous section, the equivalent impedance continues to present negative damping characteristics in the high-frequency band, and the system still faces the risk of HFR occurrence. Next, a novel HFR suppression strategy based on impedance reshaping control is proposed. A schematic of the impedance reshaping control strategy is shown in Fig. 15. The strategy includes inserting the nonlinear filter in the voltage feed-forward path and adopting an additional damping controller G_{damp} in the current loop.

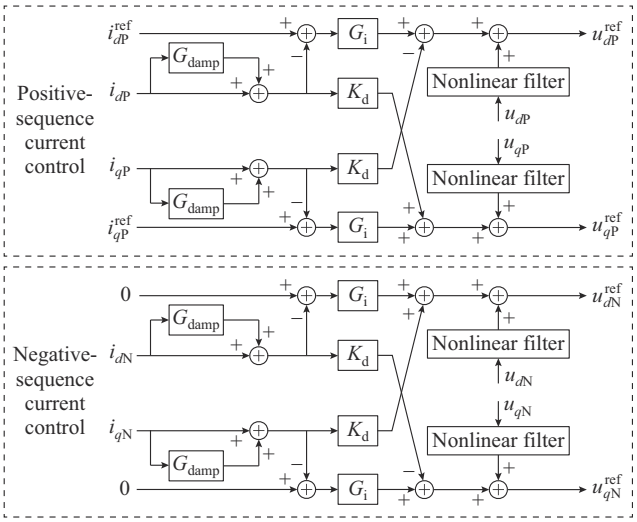

Fig. 15. Schematic of impedance reshaping control strategy.

A. Nonlinear Filter

Inserting an LPF in the voltage feed-forward path deteriorates the impedance characteristics at the middle frequency. Therefore, a novel nonlinear filter is proposed in [7], which aims to eliminate the effects of time delay on the voltage feed-forward path. The principle of a nonlinear filter is described in detail in [7], and its control flow is shown in Fig. 16.

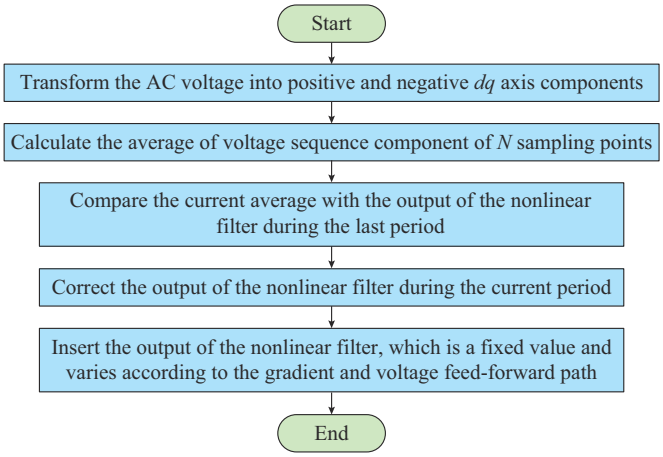

Fig. 16. Control flow chart of nonlinear filter.

The nonlinear filter adopts a hysteresis comparator and uses a close fixed feed-forward value based on the amplitude of the AC voltage. Only when the difference between the current voltage and feed-forward voltage sequence components in the last period is greater than the preset threshold can the output feed-forward voltage be updated; otherwise, the original output voltage is maintained.

According to the modeling method described in Section IV, after the nonlinear filter is adopted, the MMC self-impedance can be expressed as:

$$Z_{11,1}=sL+G_{\text{d}}(s)[G_{\text{i}}(s-s_1)G_{\text{sd}}(s-s_1)+G_{\text{i}}(s+s_1)G_{\text{sd}}(s+s_1)- \mathrm{j}K_{\text{d}}G_{\text{sd}}(s-s_1)+\mathrm{j}K_{\text{d}}G_{\text{sd}}(s+s_1)+A(s)G_{\text{lpf}}] \tag{23}$$

where G_{lpf} is the first-order LPF inserted into the power calculation path.

The integration link between the current loop and power loop can be ignored at high frequencies. Therefore, we obtain:

$$\begin{cases} G_{\text{i}}(f-f_1)\approx G_{\text{i}}(f+f_1)\approx K_{\text{p,i}} \\ G_{\text{PQ}}(f-f_1)\approx G_{\text{PQ}}(f+f_1)\approx K_{\text{p,pq}} \end{cases} \tag{24}$$

For G_{sd}, we have:

$$\begin{cases} G_{\text{sd}}(s-s_1)+G_{\text{sd}}(s+s_1)=1 \\ G_{\text{sd}}(s-s_1)-G_{\text{sd}}(s+s_1)=\mathrm{j}\mathrm{e}^{-\frac{T}{4}\mathrm{j}\omega} \end{cases} \tag{25}$$

When (24) and (25) are substituted into $Z_{11,1}$ in (23), $Z_{11,1}$ can be simplified as:

$$Z_{11,1}=\mathrm{j}\omega L+\left(K_{\text{p,i}}+K_{\text{d}}\mathrm{e}^{-\frac{T}{4}\mathrm{j}\omega}\right)G_{\text{d}}+V_1K_{\text{p,i}}K_{\text{p,pq}}G_{\text{lpf}}G_{\text{d}} \tag{26}$$

B. Principle and Modeling of Impedance Reshaping Control

After the nonlinear filter is adopted, (26) still contains the delay term, and therefore, the negative damping cannot be completely eliminated. To further improve the negative damping characteristics of MMC, an additional damping controller is inserted in the current loop. The *dq*-axis components of AC current are superimposed with themselves through the damping controller G_{damp} and then input into the current loop controller. The expressions for the positive-sequence current loop are given as:

$$\begin{cases} u_{dP}^{\text{ref}} = G_{\text{i}}[i_{dP}^{*} - (1+G_{\text{damp}})i_{dP}] - (1+G_{\text{damp}})K_{\text{d}}i_{qP} \\ u_{qP}^{\text{ref}} = G_{\text{i}}[i_{qP}^{*} - (1+G_{\text{damp}})i_{qP}] + (1+G_{\text{damp}})K_{\text{d}}i_{dP} \end{cases} \tag{27}$$

According to the modeling method described in Section IV, with the impedance reshaping control, the expression of MMC self-impedance $Z_{11,2}$ is given as:

$$Z_{11,2} = Z_{11,1} + Z_{\text{damp}} \tag{28}$$

where Z_{damp} is the virtual impedance introduced by the damping controller G_{damp} and can be derived by:

$$\begin{aligned} Z_{\text{damp}} = {} & G_{\text{damp}}(s-s_1)G_{\text{sd}}(s-s_1)[G_{\text{i}}(s-s_1) - \text{j}K_{\text{d}}]G_{\text{d}} + \\ & G_{\text{damp}}(s+s_1)G_{\text{sd}}(s+s_1)[G_{\text{i}}(s+s_1) + \text{j}K_{\text{d}}]G_{\text{d}} \end{aligned} \tag{29}$$

C. Effects of Impedance Reshaping Control on Impedance Characteristics of MMC

At medium and high frequencies, let us suppose that $G_{\text{damp}}(s-s_1) = G_{\text{damp}}(s+s_1) = G_{\text{damp}}(s)$. Equation (29) can then be simplified as:

$$Z_{\text{damp}} = \left(K_{\text{p,i}} + K_{\text{d}}\text{e}^{-\frac{T}{4}\text{j}\omega}\right)G_{\text{damp}}G_{\text{d}}G_{\text{si}} \tag{30}$$

A comparison of (26) and (30) shows that the purpose of the virtual impedance Z_{damp} is to counteract the negative damping effect of $Z_{11,1}$ and reduce the influence of the time delay in $Z_{11,1}$. Therefore, G_{damp} can be designed as a band-pass filter (BPF), where the pass band should completely avoid the negative damping frequency band.

G_{damp} can be composed of a high-pass filter (HPF), an LPF, and a gain coefficient k_{s}, and can be expressed as:

$$G_{\text{damp}} = \frac{k_{\text{s}}s}{s+\omega_{\text{H}}}\frac{\omega_{\text{L}}}{s+\omega_{\text{L}}} \tag{31}$$

where ω_{H} and ω_{L} are the bandwidths of HPF and LPF, respectively.

According to the definition of the BPF bandwidth, we have:

$$\left|\frac{k_{\text{s}}\text{j}\omega}{(\text{j}\omega+\omega_{\text{H}})}\frac{\omega_{\text{L}}}{(\text{j}\omega+\omega_{\text{L}})}\right|_{\omega=\omega_{\text{b}}} = \frac{1}{\sqrt{2}} \tag{32}$$

where ω_{b} is the cutoff frequency of the BPF.

Based on the solution given in (32), we can obtain the upper and lower cutoff frequencies ω_{b1} and ω_{b2}, respectively.

Because the phase of $Z_{11,1}$ between 550 Hz and 1600 Hz is greater than 90°, to avoid the negative damping frequency band of $Z_{11,1}$ and avoid system instability at low frequencies, the bandwidth of the designed filter should satisfy the requirements:

$$\begin{cases} \omega_{\text{b1}} > 2\pi \cdot 200 \text{ rad/s} \\ \omega_{\text{b2}} < 2\pi \cdot 500 \text{ rad/s} \end{cases} \tag{33}$$

A flow of the damping controller parameter setting is presented in Fig. 17.

The initial range of the damping controller parameters is set to be $k_{\text{s}} \in [-1.5, -0.1]$, $f_{\text{H}} \in [100, 500]$Hz, and $f_{\text{L}} \in [100, 1000]$Hz, and the step lengths of k_{s}, f_{H}, and f_{L} are set to be 0.02, 20 Hz, and 20 Hz, respectively. According to the previous method, the feasible region of the damping controller parameters can be obtained, as shown in Fig. 18.

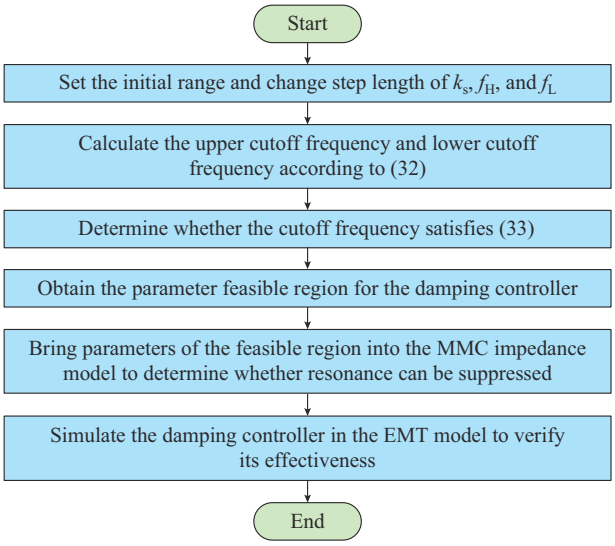

Fig. 17. Flow of damping controller parameter setting.

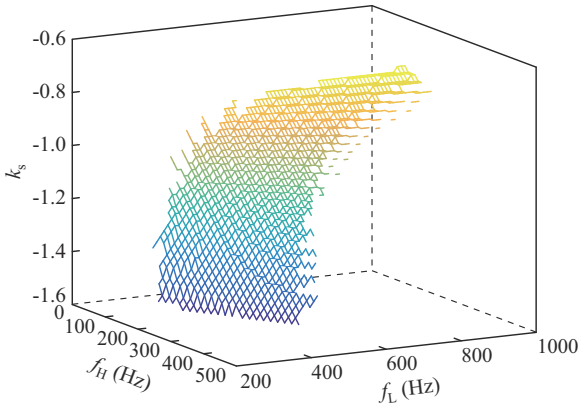

Fig. 18. Feasible region of damping controller parameters.

When the impedance characteristics of $Z_{11,2}$ are fully considered, the parameters of G_{damp} are determined to be $k_{\text{s}} = -0.8$, $f_{\text{H}} = 150$ Hz, and $f_{\text{L}} = 550$ Hz.

Figure 19 shows that the impedance reshaping control has a stronger HFR suppression capabilities than other HFR suppression strategies. Four cases are investigated.

In Case 1, the AC system is the same as in Fig. 5, and the impedance parameters are determined to be $L_{\text{g}} = 200$ mH, $C_{\text{g}} = 0.5$ μF, $R_1 = 8.4$ Ω, and $R_2 = 120$ Ω. In Cases 2 and 3, the AC system uses an AC cable with a length of 50 km. In Case 4, the length of the AC cable is 100 km.

The positive-sequence resistance, inductance reactance, and capacitance reactance are 5×10^{-5} Ω/m, 1.2×10^{-4} Ω/m, and 17 MΩ/m, respectively.

As Fig. 19 shows, the impedance characteristics of the MMC with the impedance reshaping control at the middle frequency are significantly improved, and the negative damping frequency band is further reduced compared with that using other control strategies. Note that the yellow shaded areas indicate negative damping. Cases 1 and 2 show that the impedance reshaping control has a better HFR suppression effect than the nonlinear filter control.

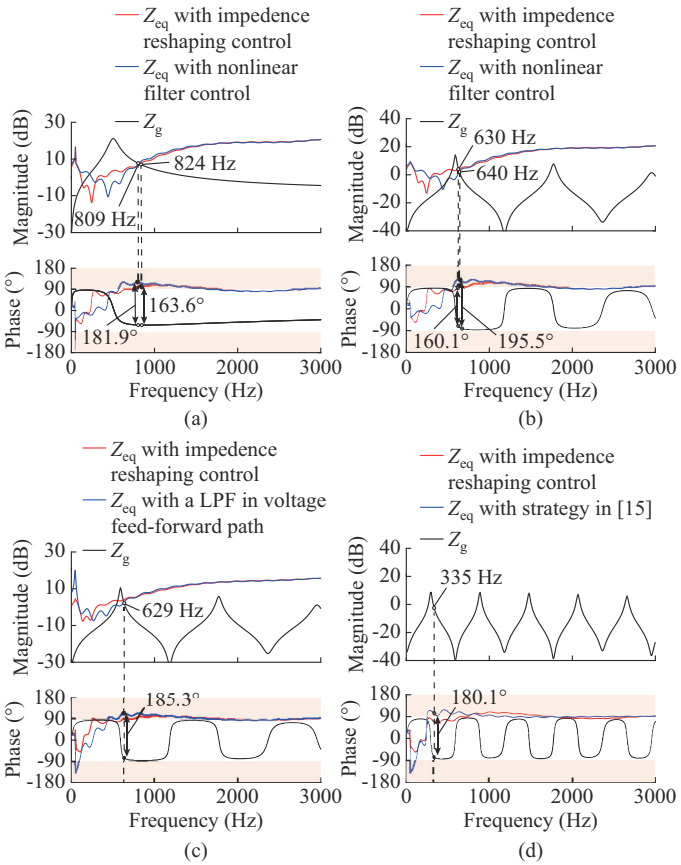

Fig. 19. Impedance characteristics of MMC and Z_g. (a) Case 1. (b) Case 2. (c) Case 3. (d) Case 4.

When only the nonlinear filter control is adopted, the amplitude of the MMC and Z_g intersect at 809 Hz and 640 Hz in Cases 1 and 2, respectively, and the corresponding phase differences are 181.9° and 195.5°, respectively. Thus, the system will resonate in both cases. After the impedance reshaping control is adopted, the corresponding phase differences between the MMC impedance and Z_g are 163.6° and 160.1° in Cases 1 and 2, respectively. Thus, the HFR is effectively suppressed.

Case 3 compares the HFR suppression effect of the impedance reshaping control and control strategy with the second-order LPF adopted in the voltage feed-forward path.

In addition, an LPF is adopted in the power outer loop. As Fig. 19(c) shows, the phase difference of Z_g and Z_{eq} with an LPF in the voltage feed-forward path is 185.3° at 629 Hz. Therefore, the system cannot remain stable.

A novel HFR suppression strategy is proposed in [15], which is achieved by adding a second-order LPF to the voltage feed-forward path and an LPF to the proportional path of the current control. The bandwidth of the LPF in the proportional path is 300 Hz. When the length of the AC cable is 50 km, both the suppression strategy in [15] and the one in this paper can maintain stability. However, as shown in Fig. 19(d), when the length is changed to 100 km, the phase difference of Z_g and Z_{eq} with the strategy in [15] is 180.1° at 335 Hz.

In the aforementioned four cases, when the impedance reshaping control is adopted, the system can maintain stability, which indicates that the impedance reshaping control has a better HFR suppression effect.

D. Verification of Effectiveness of Impedance Reshaping Control

Next, the correctness and effectiveness of the impedance reshaping control are verified by EMT simulation.

To verify the effects of time delay and impedance reshaping control, in the initial state, the system lumped delay T_d is set to be 0 μs, T_d and T_s are the same as in Table I, and another control strategy such as the nonlinear filter control is adopted. T_d step changes are from 0 to 400 μs at 1.0 s, and the impedance reshaping control is adopted after the system oscillates. Simulation results under T_d step changes are shown in Fig. 20.

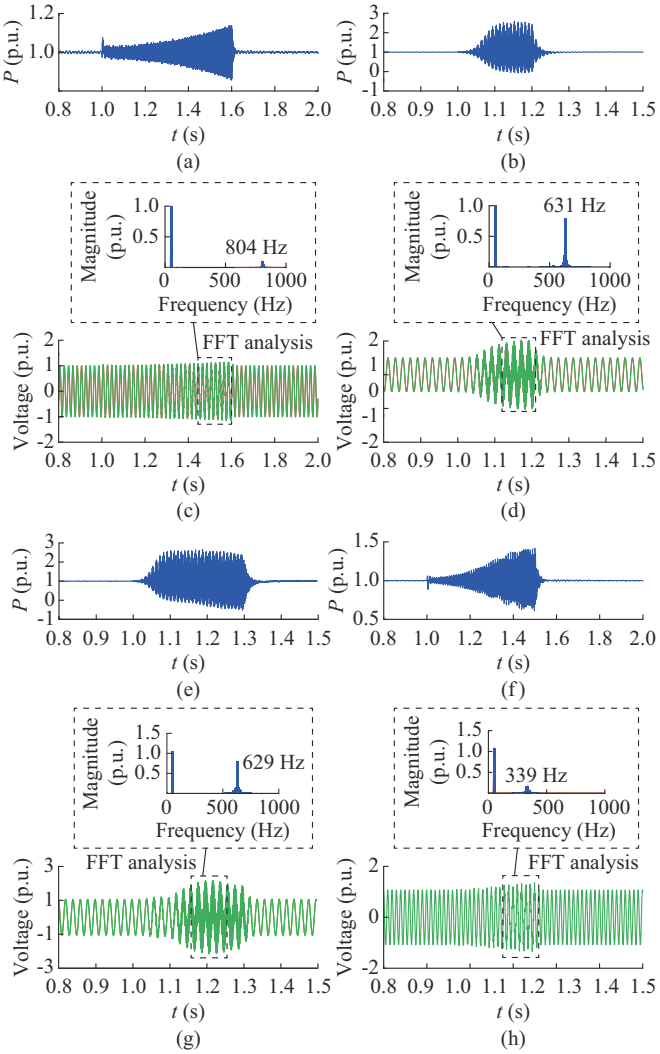

Fig. 20. Simulation results under T_d step changes. (a) Active power in Case 1. (b) Active power in Case 2. (c) Voltage at PCC in Case 1. (d) Voltage at PCC in Case 2. (e) Active power in Case 3. (f) Active power in Case 4. (g) Voltage at PCC in Case 3. (h) Voltage at PCC in Case 4.

In Cases 1 and 2, when only the nonlinear filter control is adopted, the system resonates due to the effect of the link delay. FFT analytical results of three-phase voltage show that the resonant frequencies are 804 Hz and 631 Hz in Cases 1

and 2, respectively, which are essentially the same as the analytical results presented in Fig. 19(a) and (b), respectively. In Case 3, with the increase in link delay, HFR occurs in the system, and the resonance frequency is 629 Hz, which is essentially the same as the analytical result presented in Fig. 19(c). In Case 4, before the impedance reshaping control is adopted, the HFR phenomenon cannot be suppressed, and the resonance frequency is 339 Hz, which is essentially the same as the analytical result presented in Fig. 19(d).

After impedance reshaping control is adopted, the resonance disappears in all four cases, which verifies the HFR suppression capabilities of the impedance reshaping control.

Figure 21 shows the transient performance of the impedance reshaping control in Cases 1 and 2. A single-phase metal grounding fault is applied at the AC bus at 1.0 s, and the duration of the fault is 0.1 s. In addition, to verify that the impedance reshaping control has HFR suppression capabilities within a certain time-delay range, the simulations are conducted when T_d are 400 μs and 500 μs, respectively.

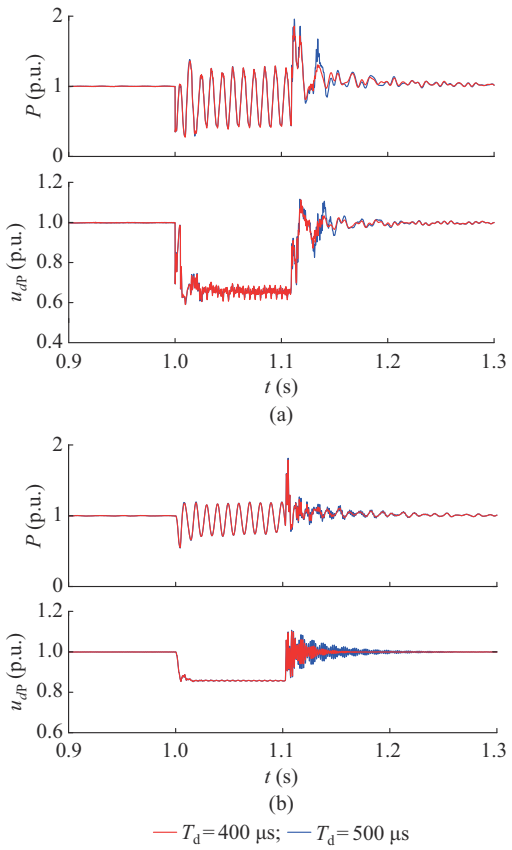

Fig. 21. Transient performance of impedance reshaping control. (a) Case 1. (b) Case 2.

Figure 21 shows that regardless of whether T_d is 400 μs or 500 μs, after the single-phase metal grounding fault is removed, the system can restore stability and has fault ride-through capabilities in both cases, thus verifying the effectiveness of the impedance reshaping control.

VII. Conclusion

In this paper, the frequency coupling impedance and equivalent SISO impedance models of MMC-HVDC systems are established, and their accuracies are verified by the impedance scanning method and EMT simulations. The analysis of the frequency characteristics of the self-impedance and coupling admittance reveals that the link delay and MMC frequency coupling significantly affect system stability. The MMC frequency coupling effect can be reduced by the proportional coefficient of the current loop or power loop. The analysis and simulations also demonstrate that inserting an LPF into the power calculation path can reduce the frequency coupling effect. To further improve the frequency characteristics of the MMC equivalent impedance and suppress the negative damping at middle and high frequencies, an impedance reshaping control strategy is proposed. HFR suppression capabilities and the transient performance of the impedance reshaping control are verified by EMT simulations in PSCAD/EMTDC.

References

[1] C. Guo, S. Yang, W. Liu *et al*., "Single-input single-output feedback control model and stability margin analysis for hybrid dual-infeed HVDC system," *IEEE Journal of Emerging and Selected Topics in Power Electronics*, vol. 9, no. 3, pp. 3061-3071, May 2021.

[2] Q. Jiang, Y. Tao, B. Li *et al*., "Joint limiting control strategy based on virtual impedance sharing for suppressing DC fault current and arm current in MMC-HVDC system," *Journal of Modern Power Systems and Clean Energy*, vol. 11, no. 6, pp. 2003-2014, Nov. 2023.

[3] C. Guo, J. Yang, C. Zhao *et al*., "Investigation of small-signal dynamics of modular multilevel converter under unbalanced grid conditions," *IEEE Transactions on Industrial Electronics*, vol. 66, no. 3, pp. 2269-2279, Apr. 2018.

[4] S. Zhu, K. Liu, L. Qin *et al*., "Analysis and suppression of DC oscillation caused by DC capacitors in VSC-based offshore island power supply system," *IEEE Transactions on Electrical and Electronic Engineering*, vol. 14, no. 4, pp. 545-555, Apr. 2019.

[5] H. Saad, Y. Fillion, S. Deschanvres *et al*., "On resonances and harmonics in HVDC-MMC station connected to AC grid," *IEEE Transactions on Power Delivery*, vol. 32, no. 3, pp. 1565-1573, Jun. 2017.

[6] C. Zou, H. Rao, S. Xu *et al*., "Analysis of resonance between a VSC-HVDC converter and the AC grid," *IEEE Transactions on Power Electronics*, vol. 33, no. 12, pp. 10157-10168, Dec. 2018.

[7] X. Guo, B. Liu, H. Mei *et al*., "Analysis and suppression of resonance between YU-E VSC-HVDC project and AC grid," *Automation of Electric Power Systems*, vol. 44, no. 20, pp. 157-164, Oct. 2020.

[8] C. Buchhagen, C. Rauscher, A. Menze *et al*., "BorWin1-first experiences with harmonic interactions in converter dominated grids," in *Proceedings of International ETG Congress 2015*, Bonn, Germany, Jun. 2015, pp. 1-7.

[9] Q. Hao, Z. Li, F. Gao *et al*., "Reduced-order small-signal models of modular multilevel converter and MMC-Based HVDC grid," *IEEE Transactions on Industrial Electronics*, vol. 66, no. 3, pp. 2257-2268, Mar. 2019.

[10] J. Freytes, G. Bergna, J. Suul *et al*., "Improving small-signal stability of an MMC with CCSC by control of the internally stored energy," *IEEE Transactions on Power Delivery*, vol. 33, no. 1, pp. 429-439, Feb. 2018.

[11] C. Guo, J. Yang, and C. Zhao, "Investigation of small-signal dynamics of modular multilevel converter under unbalanced grid conditions," *IEEE Transactions on Industrial Electronics*, vol. 66, no. 3, pp. 2269-2279, Mar. 2019.

[12] L. Xu, C. Guo, Y. Peng *et al*., "Small signal model of VSC-HVDC considering the impact of time delay," in *Proceedings of 2020 10th International Conference on Power and Energy Systems (ICPES)*, Niagara, Canada, Dec. 2020, pp. 286-291.

[13] L. Jing, Z. Xin, C. Xu *et al*., "Harmonic state-space based small-signal impedance modeling of modular multilevel converter with consideration of internal harmonic dynamics," *IEEE Transactions on Power Electronics*, vol. 34, no. 3, pp. 2134-2148, May 2019.

[14] M. Cespedes and J. Sun, "Impedance modelling and analysis of grid-connected voltage-source converters," *IEEE Transactions on Power*

Electronics, vol. 29, no. 3, pp. 1254-1261, Mar. 2014.
[15] J. Zhu, J. Hu, L. Lin *et al*., "High-frequency oscillation mechanism analysis and suppression method of VSC-HVDC," *IEEE Transactions on Power Electronics*, vol. 35, no. 9, pp. 8892-8896, Sept. 2020.
[16] X. Guo, Z. Liu, Y. Li *et al*., "Characteristic analysis of high-frequency resonance of flexible high voltage direct current and research on its damping control strategy," *Proceedings of the CSEE*, vol. 40, no. 1, pp. 19-29, Jan. 2020.
[17] J. Feng, C. Zhou, S. Yang *et al*., "Accurate impedance modeling and characteristic analysis of VSC-HVDC system for mid and high-frequency resonance problems," *Proceedings of the CSEE*, vol. 40, no. 15, pp. 4805-4819, Aug. 2020.
[18] K. Ji, H. Pang, Z. He *et al*., "Active/passive method-based hybrid high-frequency damping design for MMCs," *IEEE Journal of Emerging and Selected Topics in Power Electronics*, vol. 9, no. 5, pp. 6086-6098, Oct. 2020.
[19] M. Bakhshizadeh, "Couplings in phase domain impedance modeling of grid-connected converters," *IEEE Transactions on Power Electronics*, vol. 31, no. 10, pp. 6792-6796, Oct. 2016.
[20] G. Wang, X. Du, Y. Shi *et al*., "Mechanism analysis and stabilization of three-phase grid-inverter systems considering frequency coupling," *Journal of Power Electronics*, vol. 18, no. 3, pp. 853-862, May 2018.
[21] J. Sun, G. Wang, X. Du *et al*., "A theory for harmonics created by resonance in converter-grid systems," *IEEE Transactions on Power Electronics*, vol. 34, no. 4, pp. 3025-3029, Apr. 2019.
[22] J. Yu, X. Lin, D. Song *et al*., "New perspectives on stability analysis of three-phase grid-connected inverter considering system couplings," *IEEE Transactions on Power Systems*, vol. 35, no. 3, pp. 1967-1978, May 2020.
[23] X. Zou, X. Du, G. Wang *et al*., "Single stationary domain equivalent inverter admittance for three-phase grid-inverter system considering the interaction between grid and inverter," *Power Electronics*, vol. 12, no. 6, pp. 1593-1602, Mar. 2019.
[24] Y. Xu, H. Nian, T. Wang *et al*., "Frequency coupling characteristic modeling and stability analysis of doubly fed induction generator," *IEEE Transactions on Energy Conversion*, vol. 33, no. 3, pp. 1475-1486, Sept. 2018.
[25] S. Song, Z. Wei, Y. Lin *et al*., "Impedance modeling and stability analysis of PV grid-connected inverter systems considering frequency coupling," *CSEE Journal of Power and Energy Systems*, vol. 6, no. 2, pp. 279-290, Jun. 2020.
[26] B. Hu, H. Nian, M. Li *et al*., "Impedance characteristic analysis and reshaping method of DFIG system based on DPC without PLL," *IEEE Transactions on Industrial Electronics*, vol. 68, no. 10, pp. 9767-9777, Oct. 2021.
[27] B. Hu, H. Nian, J. Yang *et al*., "High-frequency resonance analysis and reshaping control strategy of DFIG system based on DPC," *IEEE Transactions on Power Electronics*, vol. 36, no. 7, pp. 7810-7819, Jul. 2021.
[28] H. Wu and X. Wang, "Dynamic impact of zero-sequence circulating current on modular multilevel converters: complex-valued AC impedance modeling and analysis," *IEEE Journal of Emerging and Selected Topics in Power Electronics*, vol. 8, no. 2, pp. 1947-1963, Mar. 2020.
[29] J. Man, X. Xie, S. Xu *et al*., "Frequency-coupling impedance model based analysis of a high-frequency resonance incident in an actual MMC-HVDC system," *IEEE Transactions on Power Delivery*, vol. 35, no. 6, pp. 2963-2971, Dec. 2020.

Juanjuan Wang received the M. S. degree from Huazhong University of Science and Technology, Wuhan, China, in 2003, and the Ph.D. degree from South China University of Technology, Guangzhou, China, in 2009. She is currently working as a Professor in South China University of Technology. Her research interests include flexible AC transmission system (FACTS), power system analysis and voltage stability, and operation of power systems.

Wei Chen received the B.S. degree from Southwest Jiaotong University, Chengdu, China, in 2018, and the M.S. degree from South China University of Technology, Guangzhou, China, in 2021. He is currently working in Guangdong Power Grid Co., Ltd., Guangzhou, China. His research interests include power system analysis, voltage stability, and modular multilevel converter high-voltage direct current (MMC-HVDC).

Yuekun Liu received the B.S. degree in South China University of Technology, Guangzhou, China, in 2020. He is currently pursuing the Ph.D. degree in South China University of Technology. His research interests include power system analysis and voltage stability of MMC-HVDC.

Chuang Fu received the B. S. degree from hydro-electrical engineering from Sichuan Institute of Technology, Chengdu, China, in 1996, and the M. S. and Ph.D. degrees in electrical engineering from Huazhong University of Science and Technology, Wuhan, China, in 1999 and 2003, respectively. He is currently working in the Electric Power Research Institute, China Southern Power Grid, Guangzhou, China. His research interests include FACTS, power system analysis and voltage stability, and operation of power systems.

Yunming Ye received the B.S. and M.S. degrees from South China University of Technology, Guangzhou, China, in 2019 and 2022, respectively. He is currently working in Guangdong Power Grid Co., Ltd., Guangzhou, China. His research interests include power system analysis, voltage stability, and line-commutated converter high-voltage direct current (LCC-HVDC).

Junjie Feng received the B.S. and the M.S. degrees from South China University of Technology, Guangzhou, China, in 2016 and 2019, respectively. He is currently working in the Electric Power Research Institute, China Southern Power Grid, Guangzhou, China. His research interests include power system analysis, voltage stability, and MMC-HVDC.